



Large volcanic eruptions are mostly sourced above mobile basal mantle structures



Annalise Cucchiaro ¹✉, Nicolas Flament ¹, Maëlis Arnould ² & Noel Cressie ³

Most deep mantle plumes rise from hot basal mantle structures, creating large volcanic eruptions at Earth's surface. In previous studies, mantle plumes were the implicit process connecting volcanic eruptions to hot basal mantle structures. Here, we investigate the spatiotemporal links between volcanic eruptions, hot basal mantle structures, and explicitly modelled plume conduits from 300 million years ago. We consider three volcanic eruption databases, four tomographic models and six global mantle flow models. Through Monte Carlo significance testing we find a statistical-dependence relationship between modelled plume conduits and an eruption database containing both plume head and plume tail products. We show that these eruptions, if reconstructed above the exterior of basal mantle structures, are related to the edges of fixed basal mantle structures in one tomographic model, and to the edges of mobile basal mantle structures 1% to 1.6% denser than the surrounding mantle in mantle flow models.

Large volcanic eruptions are the main surface expressions of deep mantle plumes^{1,2}, which are thought to originate from large hot basal mantle structures. Two large antipodal structures called Large Low Shear Velocity Provinces or LLSVPs have been imaged by seismic tomography at the base of the mantle under Africa and the Pacific Ocean³. A reconstruction of kimberlites and Large Igneous Provinces (LIPs) to their eruption location from 300 Ma revealed a relationship with the location of LLSVPs⁴ (Fig. 1a). This is used to claim that large hot basal mantle structures may have remained in the current configuration of seismically imaged LLSVPs for hundreds of millions of years⁴. Statistically significant relationships have been proposed to exist between LIPs and either a plume generation zone within $7^\circ \pm 5^\circ$ of LLSVP edges^{4,5} or to LLSVP interiors^{6,7}.

Mantle flow models have revealed that (1) sinking slabs shape hot basal mantle structures (model features that we propose to call 'Big Lower-mantle Basal Structures'—BLOBS), causing BLOBS to be mobile over tens of millions of years⁸ and (2) that both the edges and interiors of BLOBS are statistically related to reconstructed LIP and kimberlite eruption locations through time⁹.

Mantle plumes are conduits through which mantle 150–300 K hotter than ambient¹⁰ rises from a deep thermal instability¹¹ (Figs. 1b and 2a, b). Mantle plume conduits have a diameter of 100–200 km (ref. 12) in the upper mantle, and >600 km in the lower mantle¹³, as revealed by tomographic models at present. Some plume conduits at present are revealed by seismic

tomography to be tilted in the upper mantle¹⁴. For earlier times, deep mantle plumes may be inferred from high $^3\text{He}/^4\text{He}$ in associated mafic rocks¹⁵, such as those present in Hawaii and Samoa¹⁶. While a plume head with diameter up to 2500 km (ref. 11) may form and exist for a few million years after a mantle plume first reaches the base of the lithosphere, hot spot trails imply that plume conduits can persist for at least 100 Myr (ref. 13). The surface expression of transient mantle plume heads are large volcanic eruptions¹⁷, and smaller igneous provinces may be associated with longer-lived plume tails¹⁸. Indeed, while the most common definition of LIPs refers to mainly mafic and ultramafic igneous provinces of volume >0.1 Mkm³ and total eruption duration up to ~50 Myr, in magmatic pulses of duration ≤ 5 Myr (ref. 17), alternative definitions account for silicic volcanism² or plume 'head' and 'tail' products¹⁹ of aerial extent >0.1 Mkm² (ref. 20) and duration between ~0.5 and 1 Myr. Here we use the expression 'large volcanic eruptions' to refer to igneous provinces recorded in distinct databases^{5,19,21}.

Previous studies^{4–9} investigated the relationships between LIP and kimberlite eruptions, and LLSVPs (the fixed, present-day shape of seismically defined basal structures) or BLOBS (mobile modelled basal structures) assuming that volcanic eruptions were the product of implicit mantle plumes rising vertically from BLOBS. In these studies, large volcanic eruptions have been proposed to be linked either to LLSVP edges^{4,5,9} or LLSVP interiors^{6,7,9}. Here, we use recent reconstructions of past mantle flow that predict mobile BLOBS and mantle plumes⁹ that may be tilted¹² to

¹Environmental Futures, School of Science, University of Wollongong, Wollongong, NSW, Australia. ²Université Claude Bernard Lyon 1, École Normale Supérieure de Lyon, CNRS, Université Jean Monnet, LGL-TPE, UMR 5276, Villeurbanne, France. ³NIASRA, School of Mathematics and Applied Statistics, University of Wollongong, Wollongong, NSW, 2522, Australia. ✉e-mail: ac576@uowmail.edu.au

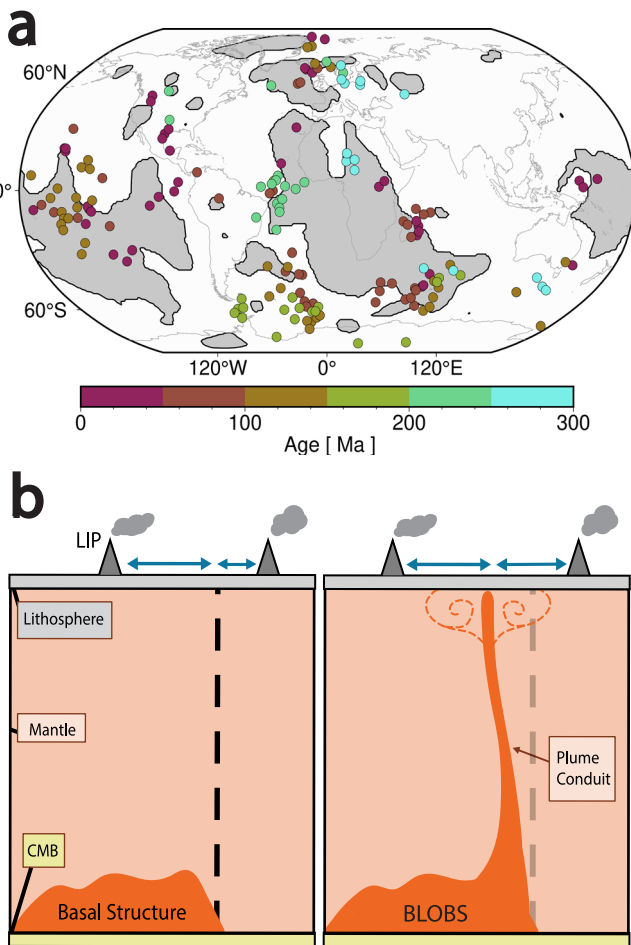


Fig. 1 | Spatiotemporal relationships between volcanic eruptions, basal mantle structures, and mantle plumes. **a** High-velocity (white) and low-velocity (grey) regions revealed by cluster analysis of tomographic model Savani²⁶ between 1000 and 2800 km depth³³, with edges outlined with a solid black line. Volcanic eruptions in J18¹⁹ reconstructed to their location at the time of eruption using a tectonic reconstruction in the no-net-rotation frame of reference^{9,30} are shown as discs coloured by age from 300 Ma. Robinson projection at Earth's surface. **b** Schematic of spatial relationships between basal mantle structures and volcanic eruptions with assumed mantle plumes as in previous work^{4–7,9} (left) and with explicit mantle plumes as in this study (right), where blue arrows represent the distance between LIPs and respective features. The schematic is not drawn to scale.

explicitly consider the relationships between large volcanic eruptions, BLOBS and modelled plumes (Figs. 1b and 2a–d).

We investigate the statistical relationships between modelled plume conduit locations and modelled BLOBS mapped using cluster analysis, and the statistical relationships between reconstructed large volcanic eruptions and the location of modelled mantle plume conduits, LLSVPs and BLOBS. As in previous work⁵, we separate large volcanic eruptions and model plume conduits according to their position above the interior or exterior of large hot basal structures. This approach makes it possible to test whether model plumes and reconstructed eruption locations that are exterior to large hot basal structures are likely to be associated with hot basal structures when accounting for plume tilt.

Success metrics for predicted basal mantle structures and plume conduits

We considered the centroids of large volcanic eruptions from 300 Ma in three separate volcanic eruption databases: Doubrovine et al.⁵ (D16⁵), which consists of 26 LIPs associated with plume 'heads' representative of an updated selection of LIPs proposed to be of deep origin^{23,24}; Ernst and

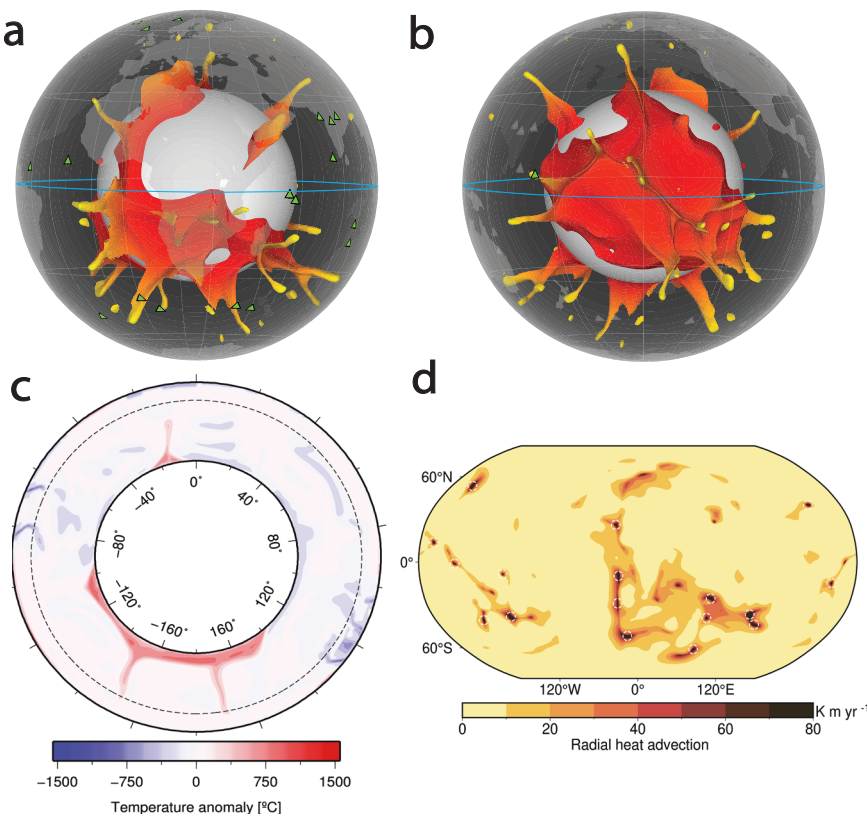
Youbi²¹ (EY17²¹), which consists of 74 mafic and silicic LIPs² associated with plume 'heads'; and Johansson et al.¹⁹ (J18¹⁹), which includes 167 volcanic products associated with both plume 'heads' and 'tails'²⁵ (see the "Methods" section and Fig. 1a).

To investigate the link between volcanic eruptions and mantle structures, we considered four S-wave tomographic models^{26–29} (T1–T4) and six forward mantle flow model cases (C1–C6). These six cases were selected based on success metrics from a series of 22 cases in ref. 9, where the initial model age, tectonic reconstruction used as a boundary condition, the viscosity of the basal layer, and density of the basal layer were varied. The success metrics were the fit between mantle flow model-predicted BLOBS and tomographically-imaged LLSVPs, and the proximity between mantle flow-modelled BLOBS and the reconstructed locations of kimberlites and LIPs⁹. Here we considered cases 4–9 from ref. 9 (cases C1–C6 herein) that used the tectonic reconstruction from ref. 30 in the no-net-rotation frame of reference from 1000 Ma as a boundary condition, and across which the density of the basal layer ($\delta\rho$, see the "Methods" section) varied between 0% and 2%. We focused on these cases because the fit between BLOBS and LLSVPs, and the proximity between BLOBS and reconstructed volcanic eruptions, is very sensitive to the density of the basal layer ($\delta\rho$). Investigating the effect of this parameter is of interest since seismological methods suggest that LLSVPs could be either purely thermal structures³¹ or intrinsically 0.5–1.7% denser than the surrounding mantle³². Mantle flow model C4 with $\delta\rho = 1.3\%$ was used as the reference case because it predicted BLOBS that best matched the area and location of LLSVPs at the present day (Supplementary Figs. 1 and 3).

As in previous studies^{9,33}, we used cluster analysis to map basal mantle structures in tomographic and mantle flow models (Supplementary Fig. 1), and to define their edges (see the "Methods" section). We treated regions above the interior and exterior of basal mantle structures (BLOBS or LLSVPs) separately to better understand the spatiotemporal relationships between mantle plume conduits and basal mantle structures. Instead of assuming that implicit vertical mantle plume conduits link volcanic eruptions to the deep Earth^{4–7,9}, we considered the centroid of modelled plume conduits (Fig. 2c and Supplementary Video 1) mapped from predicted radial heat advection²² (Fig. 2d) at two depths (Supplementary Video 1 and Supplementary Fig. 2). The radial heat advection J was defined as the product of positive temperature anomalies and upward velocity (Fig. 2d). Through trial and error and based on previous work²², appropriate radial heat advection thresholds were determined as $J \geq 80 \text{ K m yr}^{-1}$ at 1040 km depth and $J \geq 190 \text{ K m yr}^{-1}$ at 357 km depth. These radial heat advection thresholds resulted in a total number of modelled plume conduits comparable to the number of plume 'head' and 'tail' eruptions in database J18 for the last 120 Ma (Supplementary Fig. 4a and c). These thresholds also result in a number of new plume conduits comparable with the number of LIPs associated with plume 'heads' eruptions in databases D16 and EY17 for the last 300 Ma (Supplementary Fig. 4b and d; see the "Methods" section). The number of eruptions decreases back in time (Supplementary Fig. 4) due to the decreasing preservation potential of igneous rocks, particularly for plume tail eruptions in J18, which are largely preserved on the ocean floor and are entirely recycled within 200 Myr.

We analysed the angular distances (θ) between large volcanic eruptions and mantle structures (LLSVPs—see Fig. 1—BLOBS, and mantle plume conduits) and between modelled plume conduits and BLOBS edges (Fig. 3a) from 300 Ma to present day. We refer to distances between volcanic-eruption locations in the considered databases as 'sample' angular distances, which we compare to 'random' angular distances to carry out statistical analyses. We summarised angular distances as cumulative distribution functions that showed the normalised cumulative probability of angular distances being less than or equal to a given value. We refer to cumulative distribution functions for sample angular distances (such as the blue and orange curves in Fig. 3b) as 'sample distributions'. We generated 1000 sets of 'uniform random locations' with the same temporal distribution as volcanic eruptions in the considered database. For example, if a database contained three eruptions at 20 Ma, three distinct random point locations were

Fig. 2 | Plume detection scheme for preferred mantle flow model C4 ($\delta\rho = 1.3\%$) at 60 Ma. **a** and **b** 3D snapshots of modelled plumes and BLOBS at 60 Ma under the African (**a**) and Pacific (**b**) hemispheres, with 118 large volcanic eruptions as green triangles with black outlines, current present-day coastlines in light grey, and blue line highlighting the equator. **c** Equatorial annular cross-section of temperature anomaly. **d** Radial heat advection at 1040 km depth, with open white dashed discs centred on plume centroid locations from radial heat advection to $\geq 80 \text{ K m yr}^{-1}$. The age (60 Ma) was selected to capture more LIPs than at 0 Ma (Supplementary Fig. 4). Robinson projection at Earth's surface.



generated for that age in each of the 1000 sets of uniform random locations. We refer to the resulting cumulative distribution functions as ‘random distributions’ (1000 grey curves in each panel of Fig. 3b).

To assess the statistical significance of the relationships, we computed the P -value for a Monte Carlo significance test³⁴ based on a Kolmogorov–Smirnov statistic³⁵, where the null hypothesis is that the angular distances are the result of a sample of ‘uniform random locations’ (see the “Methods” section). Traditionally, $P < 0.05$ (or most liberally, $P < 0.1$) indicates departure from the null hypothesis³⁶, which means that the relationship inferred for a sample distribution is statistically significant. We reported the mean of all angular distances within the sample distribution (θ_s) and the grand mean of all 1000 random distributions (θ_r) to compare results for different model cases.

Results and discussion

Relationships between modelled plumes and BLOBS for preferred model case C4

We first assessed the statistical relationship between modelled plume conduits at 1040 km depth and modelled BLOBS for our preferred mantle flow model case C4 (Fig. 3b, Supplementary Video 2). There were more mantle plumes above BLOBS interiors (the total number of sample plume conduits for all times n_s was equal to 238; see Supplementary Fig. 4a) than above BLOBS exteriors ($n_s = 49$) from 300 Ma. In contrast, the average number of uniform random locations from 1000 tests was larger above C4 BLOBS exteriors ($n_r = 197$) than those above interiors ($n_r = 90$) from 300 Ma. This first-order result highlights the close relationship between BLOBS and mantle plume conduits.

We found no statistical-dependence relationship between C4 modelled plume conduits above C4 BLOBS interiors and C4 BLOBS edges ($\theta_s = 10^\circ$; $2^\circ < \theta_r < 8^\circ$; $P = 0.99$; Fig. 3b), indicating that modelled plume conduits above BLOBS interiors are not preferentially associated with BLOBS edges in our preferred model case. In contrast, C4 plume conduits above C4 BLOBS exteriors were strongly associated with C4 BLOBS edges ($\theta_s = 5^\circ$; $6^\circ < \theta_r < 13^\circ$; and $P = 0$). This can be explained by: (1) the

relatively large area of BLOBS exteriors (Fig. 3b and Supplementary Fig. 1), (2) the preferential association of plume conduits with BLOBS (Fig. 2c, d and Supplementary Video 4), and (3) plume tilting by a few degrees. We found modelled plume conduits in our models to be deflected on average by 2° – 5° between 1040 and 357 km depths when ascending through the mantle (Figs. 1b and 2a–c, Supplementary Videos 1, 3 and 4), which is consistent with previous work²².

Relationships between modelled plumes and BLOBS for all model cases

Extending the analysis between modelled plumes and BLOBS to mantle flow cases C1–C6 confirmed that there were systematically more mantle plumes above BLOBS interiors ($188 \leq n_s \leq 224$) than above BLOBS exteriors ($27 \leq n_s \leq 122$) (Supplementary Fig. 5a). Modelled plume locations above BLOBS exteriors (white discs in Figs. 3a and 4a) were on average approximately 5° away from BLOBS edges for all models, which was closer than uniform random point locations ($9^\circ < \theta_r < 14^\circ$, blue open discs in Fig. 4b). Modelled plume locations above BLOBS exteriors were statistically related to BLOBS edges ($P = 0$ for all six models, Fig. 4c, Supplementary Figs. 2c and 5a). In contrast, modelled plume locations above BLOBS interiors (Figs. 3a and 4a, in orange) presented no statistical relationship with BLOBS edges ($P > 0.5$, Fig. 4c, Supplementary Figs. 2c and 5a). Together, these results indicate that most model mantle plumes were above BLOBS interiors and that the mantle plumes above BLOBS exteriors were close to BLOBS edges. This result is consistent with previous studies investigating the relationship between mantle plumes and BLOBS in mantle flow models, in which plumes form where BLOBS topography is high (Fig. 2a, b and ref. 37) and sometimes migrate towards BLOBS centres due to slab push³⁸ (Supplementary Videos 1, 2, and 5 and ref. 38).

Relationships between volcanic eruptions and mantle plumes for preferred model case C4

To verify that our models predict mantle plumes at locations broadly consistent with the geological record, we quantified the distance between

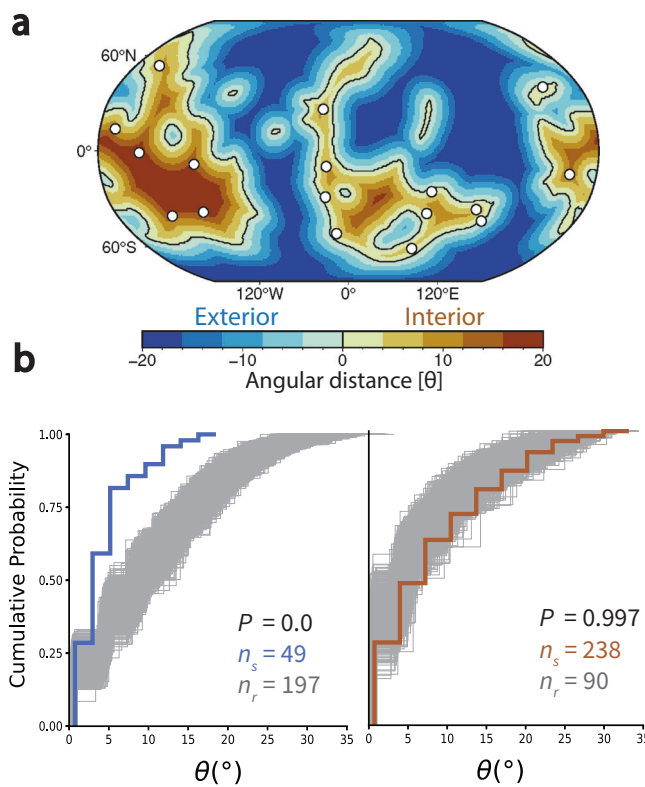


Fig. 3 | Distances between plume conduits and BLOBS for preferred mantle flow model case C4. **a**, Angular distances from C4 BLOBS edges, with C4 plume conduits superimposed as white discs at 1040 km depth and 60 Ma. Distances are positive above BLOBS interiors and negative above BLOBS exteriors following ref. 5, and they are projected to the surface. Robinson projection at Earth's surface. **b**, Cumulative distribution of distances between C4 BLOBS edges and C4 plume conduits located above the interior ($n_s = 238$, orange line) or exterior ($n_s = 49$, blue line) of C4 BLOBS, and the average number from 1000 tests (n_r) of uniform random locations (with same temporal resolution as plume conduits) above BLOBS exteriors (left panel, $n_r = 197$) and BLOBS interiors (right panel, $n_r = 90$) from 300 Ma. In **b** is the probability value (or P -value) for the Monte Carlo significance test, n_s is the number of volcanic eruptions in the sample, and n_r is the average number of uniform random locations from 1000 tests, where each test contains uniform random locations with the same temporal resolution as J18 eruptions.

large volcanic eruptions and modelled plume conduit locations for our preferred mantle flow model case C4 (Fig. 5a, b and Supplementary Video 6). This revealed a statistical-dependence relationship between J18 volcanic eruptions and C4 plume conduits (Fig. 5b, $P = 0.014$, $\theta_s = 18.5^\circ$, and $\theta_r = 22.8^\circ$). The mean angular distance between volcanic eruption locations and plume conduits was large ($\theta_s = 18.5^\circ$, Fig. 5b), which reflects that the area covered by modelled mantle plume conduits was small (for example, the C4 plume conduits shown in Fig. 5a covered 0.003% of the area at 1040 km depth at 60 Ma). As they rise towards the base of the lithosphere, mantle plume conduits form plume heads with diameters up to ~ 2500 km (ref. 39), which corresponds to an angular distance of 22.7° . This suggests that the predicted locations of modelled mantle plumes (at either 1040 or 357 km depth, Supplementary Fig. 2) are broadly consistent with J18 volcanic eruptions.

Relationships between volcanic eruptions and mantle plumes for all model cases

In all mantle flow models (C1–C6), large volcanic eruptions were closer to plume conduits ($14^\circ < \theta_s < 25^\circ$; Fig. 6a) than uniform random locations ($22^\circ < \theta_r < 25^\circ$; Fig. 6b). There was a statistical-dependence relationship between modelled plume conduits and J18 eruptions ($0 < P < 0.03$) but not D16 eruptions ($0.15 < P < 0.45$) and EY17 eruptions ($0.15 < P < 0.95$; Fig. 6c

and Supplementary Fig. 5b). This is because J18 (containing plume ‘tails’) is more directly linked to the plume conduits detected in our models, which results in point clustering due to the motion of plates above a plume conduit (Supplementary Video 2).

Relationships between large volcanic eruptions and basal mantle structures for preferred mantle flow model case C4 and tomographic model Savani (T1)

To put our results in the context of previous work^{4–7,9}, we considered the angular distance between reconstructed large volcanic eruption locations and either fixed LLSVP or mobile BLOBS edges (Figs. 7a, 8a, and 9) for tomographic model Savani (T1), which was preferred in ref. 9, and for the preferred mantle flow model case C4.

Volcanic eruptions and LLSVPs for tomographic model Savani (T1).

The average number of uniform random locations for 1000 tests above Savani LLSPV exteriors was larger ($n_r = 118$) than the number of reconstructed eruption locations in J18 ($n_s = 90$). Conversely, the average number of uniform random locations (for 1000 tests) above Savani LLSVP interiors was smaller ($n_r = 49$) than the number of reconstructed eruption locations in J18 ($n_s = 77$). This suggests that J18 eruptions are more closely associated with Savani LLSVP interiors than random points. There was no statistical relationship between J18 eruption locations reconstructed above Savani (T1) LLSVP interiors and Savani (T1) edges ($\theta_s = 6^\circ$, $\theta_r = 7^\circ$; $P = 0.996$, Fig. 7b, orange curve). In contrast, J18 eruption locations reconstructed above Savani (T1) LLSVP exteriors (Fig. 7b, blue curve) were statistically related to Savani (T1) edges ($\theta_s = 7^\circ$, $\theta_r = 10^\circ$; and $P = 0.039$, Fig. 7b, Supplementary Fig. 6, and Supplementary Video 7).

Volcanic eruptions and BLOBS for preferred mantle flow model case C4.

The number of eruption locations reconstructed above the interior ($n_s = 61$) and exterior ($n_s = 106$) of C4 BLOBS in database J18 from 300 Ma was identical to the average number of uniform random locations (from 1000 tests) reconstructed above the interior ($n_r = 61$) and exterior ($n_r = 106$) of C4 BLOBS from 300 Ma. This suggests that J18 eruptions are as closely associated with C4 BLOBS interiors as random points. J18 volcanic eruption locations reconstructed above C4 BLOBS exteriors (Fig. 8a, blue regions) were statistically related to C4 BLOBS edges ($\theta_s = 5.6^\circ$, $\theta_r = 8^\circ$ and $P = 0.05$; Fig. 8b, blue curve; Supplementary Fig. 6). In contrast, J18 volcanic eruptions reconstructed above C4 BLOBS interiors (Fig. 8a, orange regions) presented no statistical relationship with C4 BLOBS edges ($\theta_s = 10^\circ$, $\theta_r = 8^\circ$ and $P = 0.7$; Fig. 8b, orange curve; Supplementary Fig. 6).

Relationships between large volcanic eruptions and basal mantle structures for all model cases

Volcanic eruptions and LLSVPs for all tomographic model cases.

Extending the analysis to all volcanic eruption databases and tomographic model cases confirmed that the mean angular distance between volcanic eruption locations and LLSVPs for all tomographic model cases was small for both samples ($4^\circ \leq n_s \leq 12^\circ$) (Fig. 9a, Supplementary Figs. 9, 10 and 11a), and uniform-random distributions ($7^\circ \leq n_s \leq 11^\circ$) (Fig. 9b, Supplementary Figs. 9, 10 and 11b). This reflected that the fractional area covered by LLSVPs imaged as clusters between 1000 and 2800 km was relatively large for all tomographic model cases (30–52%, Supplementary Fig. 3a).

The factors controlling the number of points above LLSVP interiors and the distance between points and LLSVP edges were the fractional area covered by LLSVPs (f_a), the number of LLSVPs (n_{struc}), and the tortuosity (twisted shape) of LLSVP edges, which we quantified using the perimeter to area ratio P/A . A large f_a resulted in more points (eruption from the volcanic record or random point) above LLSVPs. A large n_{struc} decreased the distance between points above LLSVP exteriors and LLSVP edges. A large P/A , which indicated tortuous LLSVP edges, tended to reduce the distance between

Fig. 4 | Summary of distances between plume conduits and BLOBS edges for all mantle flow model cases. **a**, Average minimum angular distance of plume conduit locations to BLOBS edges. **b**, Grand mean of angular distances obtained from 1,000 samples of uniform random plume conduit locations to BLOBS edges. **c**, P -values for the Monte Carlo significance tests, with grey shading indicating a departure from the null hypothesis (symmetrical logarithmic scale). In **a** and **b**, distances are shown separately for plumes above BLOBS interiors (orange) and exteriors (blue), respectively.

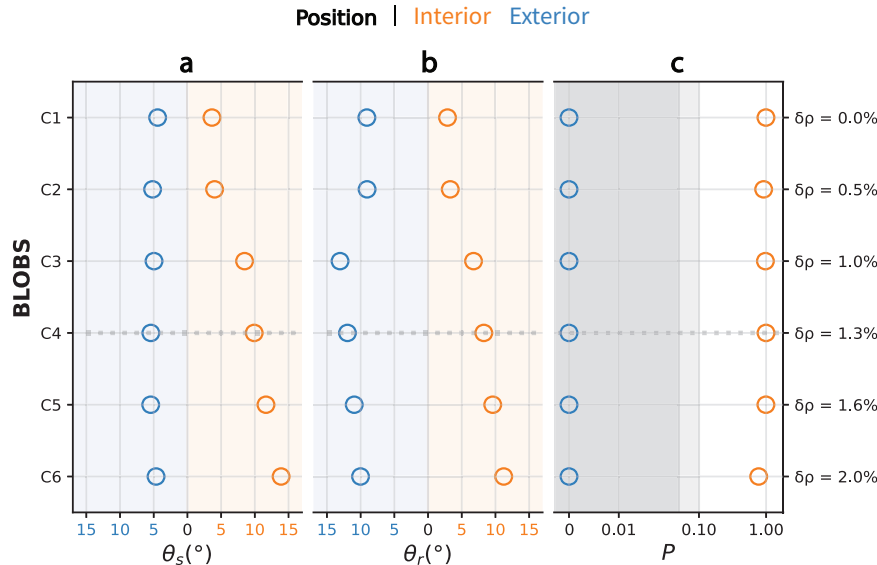
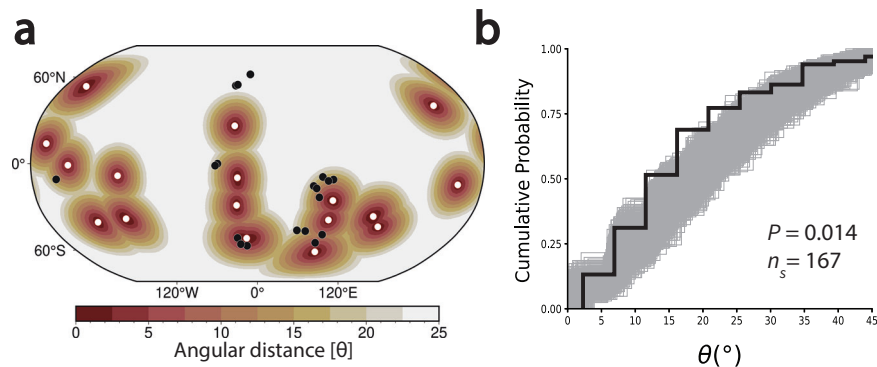


Fig. 5 | Distances between volcanic eruptions and plume conduits for preferred mantle flow model C4. **a**, Angular distance from C4 plume conduits centroids (white discs), and J18 volcanic eruptions (black discs) at 60 Ma. Robinson projection at Earth's surface. **b**, Cumulative distribution of distances to C4 plumes from 300 Ma for J18 volcanic eruptions ($n_s = 167$, black line) and for 1000 tests based on the generation of 167 uniform random locations of volcanic eruptions (grey lines). In **b**, P is the probability value (or P -value) for the Monte Carlo significance test, n_s is the number of plume conduits in the sample.



points at the surface (eruption from the volcanic record or random point) to structure edges.

There were systematically fewer volcanic eruptions above LLSVPs interiors (for J18, $69 \leq n_s \leq 80$) than above LLSVPs exteriors (for J18, $87 \leq n_s \leq 98$) (Supplementary Figs. 6–8 and 10) for three out of four tomographic model cases. In contrast, there were more large volcanic eruptions above LLSVPs interiors for GyPSuM-S²⁹ (T4) for all eruption databases, due to the large fractional area ($f_a > 50\%$) covered by GyPSuM-S LLSVPs (Fig. 10, Supplementary Figs. 1, 3, 9 and 10). For the considered tomographic models, P/A was greater for T1 (Savani), T2 (SEMUCB-WM1) than for T4 (GyPSuM-S) and T3 (S40RTS), and n_{struc} was larger for T2 (SEMUCB-WM1) and T1 (Savani) than for T3 (S40RTS) and T4 (GyPSuM-S) (Supplementary Fig. 3c). These differences in P/A and n_{struc} explained why volcanic eruptions reconstructed above LLSVP exteriors were closer from LLSVP edges for T1 (Savani) and T2 (SEMUCB-WM1) than for T3 (S40RTS) (Fig. 9a), which was the smoothest model (Fig. 10). Distances between eruption locations above GyPSuM-S LLSVPs exteriors were small because f_a was large for that tomographic model (Supplementary Fig. 3a).

A statistical-dependence relationship could only be established between J18 eruption locations reconstructed above Savani (T1) LLSVP exteriors and Savani (T1) LLSVP edges ($6^\circ < \theta_s < 7^\circ$, $10^\circ < \theta_r < 11^\circ$, $P = 0.039$, Fig. 9a–c; Supplementary Figs. 6–8). All other combinations of tomographic models and volcanic eruptions returned no statistical relationships ($P > 0.5$, Fig. 10c). Savani (T1) LLSVPs covered the smallest fractional area (Supplementary Fig. 3a) and presented the second largest

number of LLSVPs (Supplementary Fig. 3c), including some lowermost mantle structures located around $150^\circ\text{W}/30^\circ\text{N}$ and $60^\circ\text{W}/55^\circ\text{S}$, which are close to J18 eruptions (Fig. 10a) and absent in all other tomographic models (Fig. 10). The absence of significant structures in Savani (T1) around $140^\circ\text{E}/45^\circ\text{N}$ (location around which there are no reconstructed J18 eruptions) compared to other tomographic models (Figs. 1, 10a, and Supplementary Figs. 1 and 9) also contributes to this statistical-dependence relationship. Eruption locations reconstructed above LLSVPs interiors returned no statistical relationship to LLSVPs edges for any considered eruption database ($P > 0.7$ for BLOBS, Supplementary Figs. 6–8).

Volcanic eruptions and BLOBS for all mantle model cases. The mean angular distance between volcanic eruption locations and BLOBS primarily reflected the fractional area covered by BLOBS (f_a , Supplementary Fig. 3a) and the tortuosity of BLOBS edges (P/A , Supplementary Figs. 1 and 3d). The number of BLOBs in mantle flow models was systematically smaller than the number of LLSVPs in tomographic models (Supplementary Fig. 3c). The distance between eruption locations above BLOBS exteriors and BLOBS edges increased from C1 to C3 ($4.8^\circ \leq \theta_s \leq 11^\circ$, Fig. 9a) and decreased from C3 to C6 ($5.1^\circ \leq \theta_s \leq 11^\circ$, Fig. 9a), mirroring decreasing BLOBS area from C1 to C3 ($24\% \leq f_a \leq 38\%$, Supplementary Fig. 3a) and increasing BLOBS area from C3 to C6 ($24\% \leq f_a \leq 47\%$, Supplementary Fig. 3a). In contrast, the distance between eruption locations above BLOBS interiors and BLOBS edges increased with basal-layer density ($3^\circ \leq \theta_s \leq 14^\circ$, Supplementary Fig. 11a), suggesting a link to the tortuosity of BLOBS edges (P/A), which

Fig. 6 | Summary of distances between volcanic eruptions and plume conduits at 1,040 km depth for all mantle flow model cases. **a** Average minimum angular distance of eruption locations to plume-conduit locations. **b** Grand mean of angular distances obtained from 1000 samples of uniform random eruption locations to plume-conduit locations (J18, green discs; EY17 orange discs; D16 pink discs). **c** *P*-values for the Monte Carlo significance tests, with grey shading indicating a departure from the null hypothesis (symmetrical logarithmic scale). Tick labels on the right of **c** indicate the BLOBS intrinsic density anomaly (δ_p) in a given flow model.

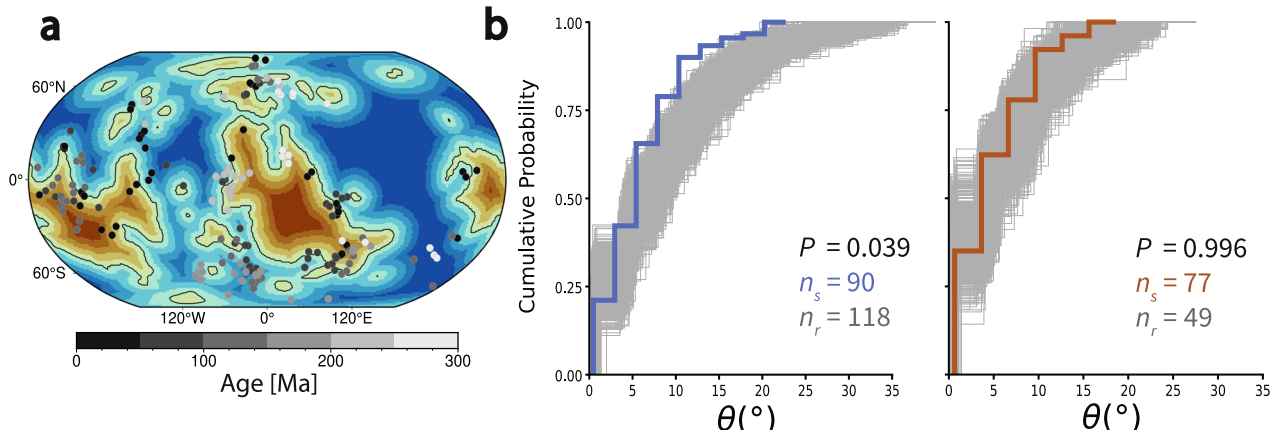
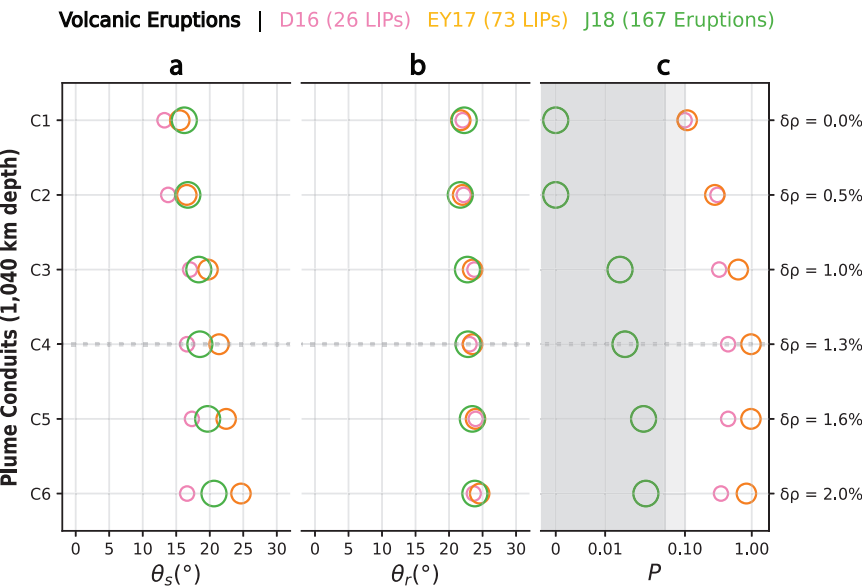


Fig. 7 | Angular distances between J18 volcanic eruptions and LLSVPs in tomographic model Savani (T1). **a** Angular distance from LLSVP edges as derived by *k*-means cluster analysis of tomographic model Savani (T1), projected to the surface (see **c** for colour scale), and J18 volcanic eruptions ($n_s = 167$) reconstructed to their eruption locations with a reconstruction³⁰ in the no-net-rotation frame of reference⁹ coloured by age from 300 Ma. Robinson projection at Earth's surface. **b** Empirical distance distributions between J18 volcanic eruptions reconstructed

above the exteriors ($n_s = 90$, blue line) or interiors ($n_s = 77$, orange line) of Savani (T1) LLSVPs, and the average number from 1000 tests (n_r) of uniform random locations (with same temporal resolution as J18 eruptions) above the exteriors (left panel, $n_r = 118$) and interiors (right panel, $n_r = 49$) of Savani LLSVPs from 300 Ma. In **b**, *P* is the *P*-value for the Monte Carlo significance test, n_s is the number of eruptions in the sample.

decreased from C1 to C6 (Supplementary Figs. 1, 3d and Supplementary Videos 8–10).

There were systematically fewer volcanic eruptions above BLOBS interiors (for J18, $49 \leq n_s \leq 72$) than above BLOBS exteriors (for J18, $95 \leq n_s \leq 118$) for mantle flow models C1–C5 (Supplementary Figs. 6–8). For case C6, fewer eruptions from databases J18 and D16 were reconstructed above BLOBS exteriors, due to the large fractional area f_a covered by C6 BLOBS (47%, Supplementary Fig. 3a). Large volcanic eruptions reconstructed above modelled BLOBS exteriors (Supplementary Videos 8–10) were closer to BLOBS ($5^\circ < \theta_s < 11^\circ$, Fig. 9a) than uniform random locations ($7^\circ < \theta_s < 13^\circ$; Fig. 9b). The *P*-value was larger than 0.10 for almost all eruption databases (Fig. 9c; Supplementary Figs. 6–8), except for cases C3–C5 (BLOBS with $1\% \leq \delta_p \leq 1.6\%$) and J18 eruptions, for which the null hypothesis could be rejected at the 10% level ($0.051 < P < 0.063$, Fig. 9c). This was because eruptions linked to plume tails were more clustered in J18 results than eruptions linked to plume heads in D16 and EY17

(Supplementary Video 2). There was some clustering of eruptions in EY17, but also some scattering possibly due to the inclusion of silicic LIPs in that database (Supplementary Video 2). Cases C3–C5, for which $P < 0.1$ (Fig. 9c), closely matched the area, location, and *P/A* of LLSVPs at the present day (Supplementary Figs. 1 and 3).

Eruption locations reconstructed above structure interiors returned no statistical relationship between eruption locations and structure edges for any considered eruption database and mantle structures ($P > 0.7$ for BLOBS, Supplementary Figs. 6–8; $P > 0.95$ for LLSVPs, Supplementary Figs. 9–11). We attribute this absence of a statistical relationship to the relatively small area of structure interiors (Supplementary Fig. 3a, $24\% \leq f_a \leq 52\%$). Because of the shape of structures⁷, here captured by *P/A* (Supplementary Fig. 3d), uniform random locations above structure interiors were as close to structure edges as sample locations (Figs. 9a, b, 10, Supplementary Figs. 9 and 10b and Supplementary Videos 8–10).

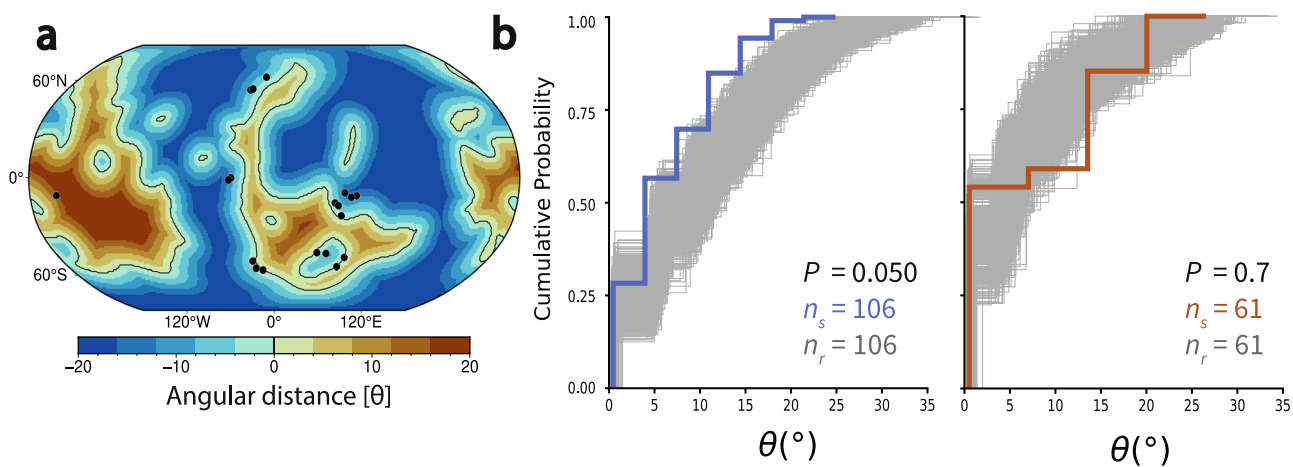


Fig. 8 | Angular distances between J18 volcanic eruptions and basal mantle structures for preferred mantle flow model case C4 and tomographic model Savani (T1). **a** Angular distance from C4 BLOBS from k -means cluster analysis, and reconstructed J18 volcanic eruptions (black dots), both at 60 Ma. Robinson projection at Earth's surface. **b** Empirical distance distribution from 300 Ma between C4 BLOBS and J18 volcanic eruptions reconstructed above BLOBS exteriors ($n_s = 106$, blue lines) or interiors ($n_s = 61$, orange line), C4 BLOBS, and the average number

from 1000 tests (n_r) of uniform random locations (with same temporal resolution as J18) above C4 BLOBS exteriors (left panel, $n_r = 106$) and C4 BLOBS interiors (right panel, $n_r = 61$) from 300 Ma. In **b**, P is the P -value for the Monte Carlo significance test, n_s is the number of eruptions in the sample, and n_r is the average number of uniform random locations from 1000 tests, where each test contains uniform random locations with the same temporal resolution of J18.

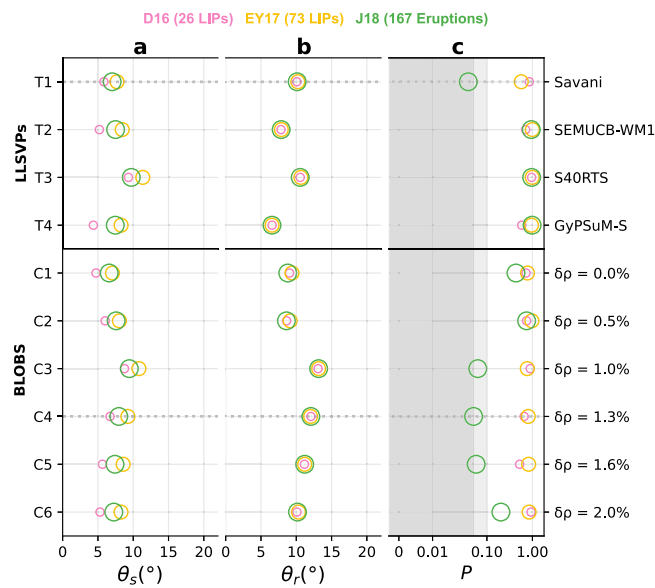


Fig. 9 | Angular distances and statistical significance for volcanic-eruption locations reconstructed above LLSVP and BLOBS exteriors for all model cases. **a** Mean minimum angular distance between large volcanic eruptions of three databases and fixed LLSVPs and mobile BLOBS edges. **b** Grand mean of angular distances obtained from 1000 samples of uniform random eruption locations with the same temporal distribution as each respective large volcanic eruption database to fixed LLSVP edges or mobile BLOBS edges from 300 Ma. **c** P -values for the Monte Carlo significance tests, with grey shading indicating departure from the null hypothesis (symmetrical logarithmic scale).

Conclusions

Our statistical analyses provide new insights into the relationships between volcanic-eruption locations, basal mantle structures, and modelled plume conduits. We found that reconstructed large volcanic eruption locations were strongly related to modelled mantle plume conduits that rise from the interior of mobile basal mantle structures. We identified statistical-dependence relationships for eruption locations associated with plume

heads and tails (J18) reconstructed above the exteriors of both Savani (T1) LLSVPs and BLOBS with intrinsic density anomaly between 1% and 1.6% greater than ambient mantle (C3–C5). The statistical-dependence relationships between eruption locations and basal mantle structures' exteriors depend on the clustering of eruptions, and on the area, number, shape, and location of basal mantle structures. Tomographic model Savani (T1) presented 22 distinct basal mantle structures, including some around 150°W/30°N and 60°W/55°S, in the vicinity of reconstructed J18 eruption locations. Mantle flow model cases C3–C5 presented basal mantle structures of fractional area and edge tortuosity comparable to tomographic models.

We treated the interiors and exteriors of basal mantle structures separately. We found that modelled plume conduits located above BLOBS exteriors were strongly related to BLOBS edges. This is consistent with models in which plumes form where BLOBS topography is high and sometimes migrate towards BLOBS centre due to slab push. In contrast, we found modelled plume conduit locations and large eruptions reconstructed above the interior of LLSVPs or BLOBS to have no significant relationship to the edges of these structures. This result supports a view in which plumes are not limited to a plume generation zone at the edge of fixed LLSVPs⁴⁵ but are instead primarily anywhere above the interior of mobile BLOBS, or within ~5° of their edges due to plume tilting.

Methods

Volcanic-eruption databases

We considered three volcanic eruption databases. Database J18¹⁹ included volcanic eruptions associated with plume heads, as well as oceanic islands and seamounts associated with longer-lived plume tails (from ref. 17). Database EY17²¹ included 74 interpreted volcanic-eruption fragments and silicic LIPs consistent with the LIP definition of ref. 2. Database D16⁵ consisted of 26 LIPs between 297 Ma and 15 Ma and represented an update of a selection of 25 LIPs proposed to be of deep origin by ref. 23 and originally mostly compiled from refs. 40,41. D16 LIPs were available as centroids. We used pyGPlates (www.gplates.org/pygplates), the application programming interface (API) for GPlates⁴², to identify the centroid of volcanic eruption polygons in databases J18 and EY17. We only considered volcanic eruptions from 300 Ma with an area extent >20,000 km² and obtained 167 volcanic eruptions for J18 and 73 volcanic eruptions for EY17.

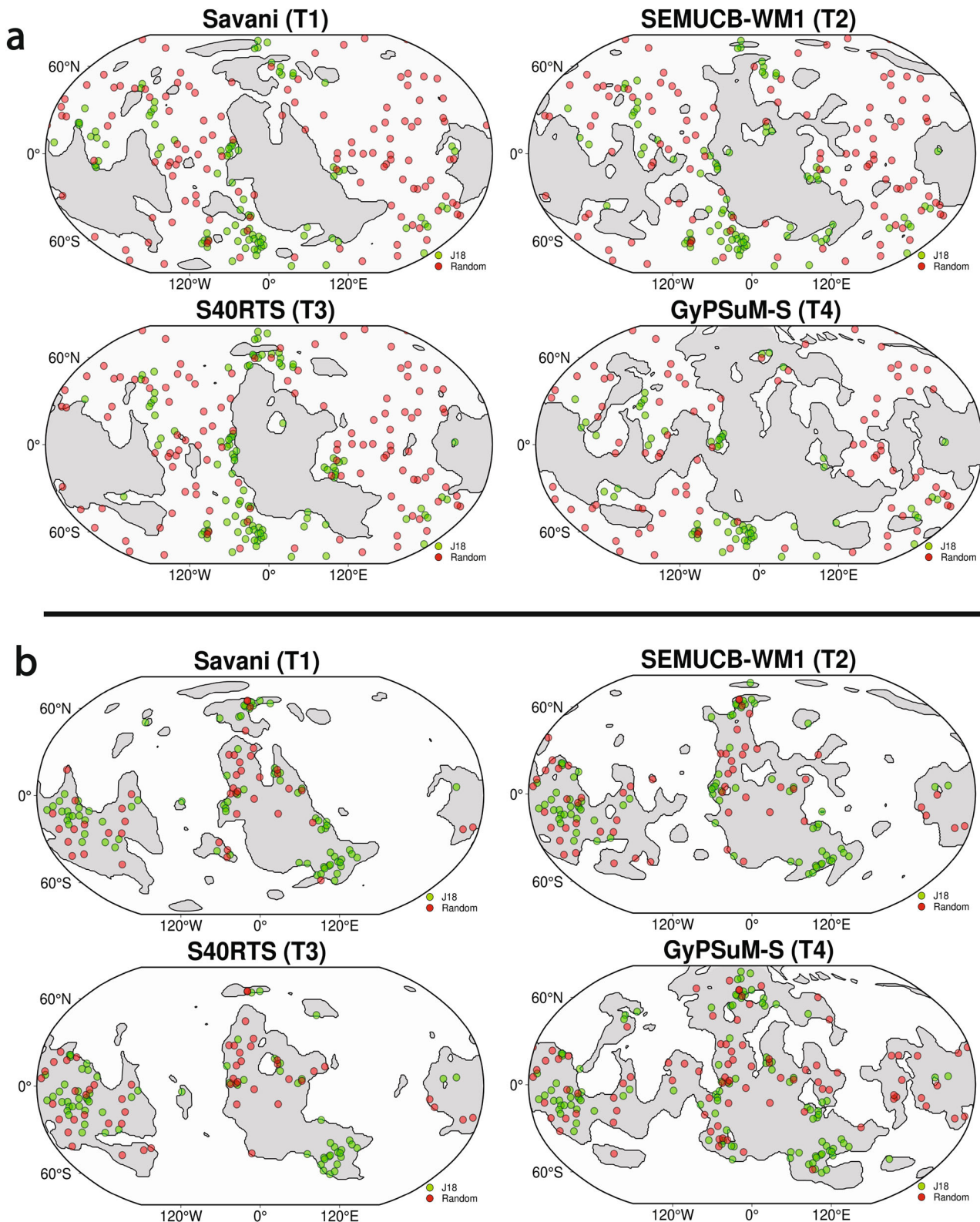


Fig. 10 | Spatial distribution of volcanic eruptions in database J18, and one set of random point locations above exteriors and interiors of LLSVPs. LLSVPs in tomographic models T1–T4 are shown in grey with edges outlined in solid black. Eruptions in database J18 from 300 Ma reconstructed above the exterior (a) and

interiors (b) of LLSVPs are shown as green discs. One set out of the 1000 sets of uniform random point locations above LLSVPs exteriors (a) and interiors (b), containing the same number of points as database J18, is shown as red discs. Robinson projection at Earth's surface.

To match the temporal increment at which we interrogate mantle flow models (see below), we resampled the volcanic eruptions in each database, assigning the age a to volcanic eruptions that occurred within

$(a - a_w) < a \leq (a + a_w)$, where $a_w = 10$ Myr was an age window. This temporal resolution was deemed appropriate because large volcanic eruptions may be emplaced over up to 50 Myr (ref. 2).

Tomographic models

We considered S-wave tomographic models Savani²⁶, SEMUCB-WM1²⁷, S40RTS²⁸, and GyPSuM-S²⁹. As in previous work (e.g., refs. 9,33) we used two-means cluster analysis to map regions with slow velocity anomalies between 1000 and 2800 km depth.

Reconstructions of past mantle flow

We reconstructed mantle flow from one billion years ago using the finite-element code CitcomS⁴³ modified to read in tectonic reconstructions⁴⁴ with continuously closing plate polygons⁴⁵. We used a tectonic reconstruction³⁰ modified to be in the no-net-rotation reference frame⁹, which is appropriate to model mantle flow⁴⁶. Indeed, the fit between predicted BLOBS and imaged LLSVPs is much better for reconstructions of past mantle flow forced with this tectonic reconstruction in the no-net-rotation reference frame than for the original tectonic reconstruction in a paleomagnetic reference frame⁹. Buoyancy-driven flow was represented by approximating Earth's mantle as an incompressible fluid under the extended Boussinesq approximation which accounts for viscous dissipation and an adiabatic temperature gradient with a decrease of the coefficient of thermal expansion with depth⁴⁷. Convective vigour was controlled by the Rayleigh number,

$$\text{Ra} = \alpha_0 \rho_0 g_0 \Delta T h^3 M / (\kappa_0 \eta_0),$$

where the subscript '0' indicates reference values. α_0 was the coefficient of thermal expansion that decreased by a factor of two over the thickness of the mantle from $\alpha_0 = 3 \times 10^{-5} \text{ K}^{-1}$ at the surface, $\rho_0 = 4000 \text{ kg m}^{-3}$ was the density, $g_0 = 9.81 \text{ m s}^{-2}$ was the gravitational acceleration, $\Delta T = 3100 \text{ K}$ was the temperature change across the mantle, $h_M = 2867 \text{ km}$ was the thickness of the mantle, $\kappa_0 = 1 \times 10^{-6} \text{ m}^2 \text{ s}^{-1}$ was the thermal diffusivity and $\eta_0 = 1.1 \times 10^{21} \text{ Pa s}$ was the viscosity. With these values, Ra was equal to 7.8×10^7 . The internal heating rate $H = 33.6 \text{ TW}$ represented heat produced by radioactive elements and from primordial accretion⁴⁸. The dissipation number was

$$\text{Di} = \alpha_0 g_0 h_M / (C_{P0}) = 0.70,$$

where $C_{P0} = 1200 \text{ J kg}^{-1} \text{ K}^{-1}$ was the mantle heat capacity.

The composition of the basal layer was modelled using tracers with buoyancy ratio

$$B = \delta\rho / (\rho\alpha\Delta T),$$

where $\rho = 5546 \text{ kg m}^{-3}$ and $\alpha = 1.32 \times 10^{-5} \text{ K}^{-1}$ were the average density and thermal expansivity within 100 km above the CMB from PREM⁴⁹ and ref. 38 respectively. The quantity B was varied between 0 and 0.5 across cases C1–C6 (which are cases C4–C9 of ref. 9), which gave $0\% \leq \delta\rho \leq 2\%$ as the average density of the basal layer in the lower-most 100 km above the CMB.

Viscosity depends on depth, composition, temperature, and pressure as

$$\begin{aligned} \eta = \eta(r)\eta_0\eta_C, \exp & \left\{ \left[E_\eta + \rho_0 g_0 Z_\eta (R_0 - r) \right] / [R(T + T_{\text{off}})] \right. \\ & \left. - \left[E_\eta + \rho_0 g_0 Z_\eta (R_0 - R_C) \right] / [R(T_{\text{CMB}} + T_{\text{off}})] \right\} \end{aligned}$$

with $\eta(r)$ equal to 0.002 in the asthenosphere (between 160 and 310 km depth), to 0.02 in the lithosphere (above 160 km depth) and between 310 and 660 km depth, and to 0.2 in the lower mantle (below 660 km depth)³⁶. Here, r was the radius and $R_C = 3504 \text{ km}$ was the radius of the core, $E_\eta = 284 \text{ kJ mol}^{-1}$ was the activation energy, $Z_\eta = 2.1 \times 10^{-6} \text{ m}^3 \text{ mol}^{-1}$ was the activation volume, $R = 8.31 \text{ J mol}^{-1} \text{ K}^{-1}$ was the universal gas constant, T was the dimensional temperature, $T_{\text{CMB}} = 3,380 \text{ K}$ was the temperature at the core-mantle boundary, and $T_{\text{off}} = 452 \text{ K}$ was a temperature offset and η_C was the compositional viscosity pre-factor equal to 1 for ambient mantle, 100 for continental lithosphere and 10 for BLOBS to obtain viscosity variations over three orders of magnitude within the range 1.1×10^{20} to

$2.2 \times 10^{23} \text{ Pa s}$. While this viscosity contrast was smaller than expected within Earth's mantle⁵⁰, it made it possible to compute time-dependent mantle flow over hundreds of millions of years. The output of mantle flow simulations was saved in 20 Myr increments and analysed from 300 Ma by two-means cluster analysis to map regions with high-temperature anomalies between 1000 and 2800 km depth.

Plume detection scheme

Several methods have been proposed to detect mantle plumes in mantle flow models, with detection schemes involving wavelet thresholding⁵¹, k -means clustering algorithms³⁷, and isolation via a large radial-heat-advection value²². We used the latter approach and detected plume conduits based on radial heat advection J , which is proportional to $v_z T$, where v_z was the positive radial velocity and T was the temperature. We mapped mantle plumes as areas with $J \geq 80 \text{ K m yr}^{-1}$ at $\sim 1040 \text{ km}$ depth and $J \geq 190 \text{ K m yr}^{-1}$ at $\sim 357 \text{ km}$ depth. We identified through trial and error that defining plumes as having radial heat advection $J \geq 80 \text{ K m yr}^{-1}$ at 1040 km depth resulted in a number of total plumes and new plumes that was consistent with observations (Supplementary Fig. 4). Indeed, there were between 3 and 16 'head' and 'tail' eruptions in database J18 (total 167 eruptions), and between 13 and 17 total modelled plume conduits in mantle flow models per 20 Myr increment from 120 Ma (total 107–139 eruptions). The decrease in the number of plumes in J18 back in time reflected the decreasing area of preserved seafloor that carries plume tail products (Supplementary Fig. 4a). There were on average four LIPs with peaks between 13 and 15 LIPs in EY17 (total 73 eruptions), and between four and six new plumes with peaks of up to 11–15 new plumes in mantle flow model cases per 20 Myr increment from 300 Ma (total 75–99 eruptions, Supplementary Fig. 4b). The plume tilt was measured as the angular distance between plume centroids at 357 km depth and the nearest plume centroid at 1040 km depth. If a new plume was detected more than 800 km from a previous plume, it was counted as a new plume and was assigned a new plume ID for the next timestep²⁰.

Evaluating model success: Match between BLOBS and LLSVPs

The extent of LLSVPs and BLOBS was mapped from k -means clustering between 1000 and 2800 km depth^{9,33}. To quantify the match between model BLOBS and LLSVPs, we first calculated the fractional area covered by LLSVP (seismically slow) clusters for the present-day, and by BLOBS (hot) clusters as an average from 300 Ma. This step was to ensure that the extent of predicted BLOBS was similar to that of imaged LLSVPs. We next quantified the spatial match between the present-day BLOBS predicted for a given model case and the LLSVPs imaged by a given tomographic model as an accuracy measure $\text{Acc} = (\text{TPA} + \text{TNA})/A$, where TPA or 'True Positive Area' indicated areas where BLOBS clusters matched LLSVP clusters, TNA or 'True Negative Area' indicated areas outside BLOBS clusters matching areas outside LLSVP clusters, and A was the entire area (Supplementary Fig. 1). For a given model case, the accuracy was averaged across all four tomographic models T1–T4, and for a given tomographic model, the accuracy was averaged across the other three tomographic models (Supplementary Fig. 3b). We verified that present-day model BLOBS covered an area similar to that of LLSVPs and quantified the geographic match between present-day BLOBS and LLSVPs (Supplementary Fig. 3).

Evaluating model success: Distance between volcanic eruptions, LLSVPs, BLOBS, and plumes

To assess the success of different models, we quantified the distance between volcanic eruptions and LLSVPs, volcanic eruptions and BLOBS, volcanic eruptions and modelled plumes, and modelled plumes and BLOBS, from 300 Ma. We created global maps of angular distances from either the edge of LLSVPs or BLOBS (Supplementary Videos 5 and 7, in which the edge is represented by a solid black line) or from mantle plumes as detected from thresholding global radial heat advection (Supplementary Video 2). The edges of BLOBS and LLSVPs were defined by cluster analysis of temperatures (for BLOBS) and seismic velocities (for LLSVPs) from 1000 to

2800 km depth as in ref. 9. These maps were then queried at reconstructed volcanic eruption locations for a given volcanic eruption database (or at modelled-plume-conduit centroid locations), and the resulting distances were cumulated from 300 Ma as sample distributions that indicated the cumulative probability of occurrence of volcanic eruptions as a function of angular distance. We reported the mean angular distance values of sample distributions θ_s , and the grand mean of those obtained from angular distance from uniform random locations, θ_r (Figs. 4, 6, and 9).

Evaluating model success: Statistical significance of distances

We carried out a type of Monte Carlo significance test³⁴. To assess the statistical significance of the relationships, 1000 sets of uniform random locations were drawn, each with the same temporal distribution as volcanic eruptions and/or plumes in the considered database/model but located uniformly and randomly on Earth's surface⁹. For a given eruption database, the same uniform random locations were used for each mantle flow model and tomographic model case. We used a two-sample Kolmogorov–Smirnov (KS) statistic³⁵, where the maximum absolute difference between the sample distribution and the empirical distribution obtained from uniform random locations is computed. We computed the probability value, or *P*-value, $P = 1 - f_{KS}/100$, where f_{KS} is the percentage (out of 1000) of empirical distributions obtained from generating uniform random locations, for which the two-sample Kolmogorov–Smirnov (KS) statistical test³⁵ rejected the null hypothesis that the sample distribution was drawn from a distribution based on uniform random locations. For example, $P = 0$ corresponds to $f_{KS} = 100\%$, indicating that the sample distribution was distinct from each empirical distribution generated by uniform random locations. The null hypothesis would traditionally be rejected at the 5% significance level for $f_{KS} > 95\%$, which corresponds to $P < 0.05$. The null hypothesis would most liberally be rejected at the 10% significance level for $f_{KS} > 90\%$, which corresponds to $P < 0.1$.

Data availability

Data and scripts used in this study are accessible at: https://figshare.com/projects/Links_between_eruptions_structures_and_plumes_supplement/217489. Figures 1a, 2c, 3a, b, 4, 5a, b, 6, 7a, b, 8a, b, 9 and 10 were created using open source python libraries PyGMT⁵² and Matplotlib⁵³.

Code availability

The version of the open-source code CitcomS used in this study is accessible at: <https://github.com/EarthByte/citcoms>.

Received: 7 October 2024; Accepted: 12 June 2025;

Published online: 09 July 2025

References

- Ernst, R. E., Buchan, K. L. & Campbell, I. H. Frontiers in Large Igneous Province research. *Lithos* **79**, 271–297 (2005).
- Bryan, S. E. & Ernst, R. E. Revised definition of Large Igneous Provinces (LIPs). *Earth-Sci. Rev.* **86**, 175–202 (2008).
- Garnero, E. J. & McNamara, A. K. Structure and dynamics of Earth's lower mantle. *Science* **320**, 626–628 (2008).
- Torsvik, T. H., Burke, K., Steinberger, B., Webb, S. J. & Ashwal, L. D. Diamonds sampled by plumes from the core–mantle boundary. *Nature* **466**, 352–355 (2010).
- Doubrovine, P. V., Steinberger, B. & Torsvik, T. H. A failure to reject: testing the correlation between large igneous provinces and deep mantle structures with EDF statistics. *Geochem. Geophys. Geosyst.* **17**, 1130–1163 (2016).
- Astermann, J., Kaye, B. T., Mitrovica, J. X. & Huybers, P. A statistical analysis of the correlation between large igneous provinces and lower mantle seismic structure. *Geophys. J. Int.* **197**, 1–9 (2014).
- Davies, D. R., Goes, S. & Sambridge, M. On the relationship between volcanic hotspot locations, the reconstructed eruption sites of large igneous provinces and deep mantle seismic structure. *Earth Planet Sci. Lett.* **411**, 121–130 (2015).
- McNamara, A. K. & Zhong, S. Thermochemical structures beneath Africa and the Pacific Ocean. *Nature* **437**, 1136–1139 (2005).
- Flament, N., Bodur, O. F., Williams, S. E. & Merdith, A. S. Assembly of the basal mantle structure beneath Africa. *Nature* **603**, 846–851 (2022).
- Putirka, K. D. Mantle potential temperatures at Hawaii, Iceland, and the mid-ocean ridge system, as inferred from olivine phenocrysts: evidence for thermally driven mantle plumes. *Geochem. Geophys. Geosyst.* **6**, 5 (2005).
- Gonnermann, H. M., Jellinek, A. M., Richards, M. A. & Manga, M. Modulation of mantle plumes and heat flow at the core–mantle boundary by plate-scale flow: results from laboratory experiments. *Earth Planet. Sci. Lett.* **226**, 53–67 (2004).
- Campbell, I. H. Testing the plume theory. *Chem. Geol.* **241**, 153–176 (2007).
- French, S. W. & Romanowicz, B. Broad plumes rooted at the base of the Earth's mantle beneath major hotspots. *Nature* **525**, 95–99 (2015).
- Tsekhnistrenko, M., Sigloch, K., Hosseini, K. & Barruol, G. A tree of Indo-African mantle plumes imaged by seismic tomography. *Nat. Geosci.* **14**, 612–619 (2021).
- Koppers, A. A. P. et al. Mantle plumes and their role in Earth processes. *Nat. Rev. Earth Environ.* **2**, 382–401 (2021).
- Mundl-Petermeier, A. et al. Anomalous 182W in high 3He/4He ocean island basalts: fingerprints of Earth's core? *Geochim. Cosmochim. Acta* **271**, 194–211 (2020).
- Ernst R. E. *Large Igneous Provinces* (Cambridge University Press Cambridge, 2014).
- Richards, M. A., Duncan, R. A. & Courtillot, V. E. Flood basalts and hot-spot tracks: plume heads and tails. *Science* **246**, 103–107 (1989).
- Johansson, L., Zahirovic, S. & Müller, R. D. The interplay between the eruption and weathering of Large Igneous Provinces and the deep-time carbon cycle. *Geophys. Res. Lett.* **45**, 5380–5389 (2018).
- Coffin, M. F. et al. Large igneous provinces and scientific ocean drilling: status quo and a look ahead. *Oceanography* **19**, 150–160 (2006).
- Ernst, R. E. & Youbi, N. How Large Igneous Provinces affect global climate, sometimes cause mass extinctions, and represent natural markers in the geological record. *Palaeogeogr. Palaeoclimatol. Palaeoecol.* **478**, 30–52 (2017).
- Arnould, M., Coltice, N., Flament, N. & Mallard, C. Plate tectonics and mantle controls on plume dynamics. *Earth Planet. Sci. Lett.* **547**, 116439 (2020).
- Burke, K. & Torsvik, T. H. Derivation of large igneous provinces of the past 200 million years from long-term heterogeneities in the deep mantle. *Earth Planet. Sci. Lett.* **227**, 531–538 (2004).
- Torsvik, T. H., Smethurst, M. A., Burke, K. & Steinberger, B. Large igneous provinces generated from the margins of the large low-velocity provinces in the deep mantle. *Geophys. J. Int.* **167**, 1447–1460 (2006).
- Millard, F. et al. Wallace Large Igneous Provinces and scientific ocean drilling: status quo and a look ahead. *Oceanography* **19**, 150–160 (2006).
- Auer, L., Boschi, L., Becker, T. W., Nissen-Meyer, T. & Giardini, D. Savani: a variable resolution whole-mantle model of anisotropic shear velocity variations based on multiple data sets. *J. Geophys. Res.: Solid Earth* **119**, 3006–3034 (2014).
- French, S. W. & Romanowicz, B. A. Whole-mantle radially anisotropic shear velocity structure from spectral-element waveform tomography. *Geophys. J. Int.* **199**, 1303–1327 (2014).
- Ritsema, J., Deuss, A., van Heijst, H. J. & Woodhouse, J. H. S40RTS: a degree-40 shear-velocity model for the mantle from new Rayleigh wave dispersion, teleseismic traveltimes and normal-mode splitting function measurements. *Geophys. J. Int.* **184**, 1223–1236 (2011).

29. Simmons N. A., Forte A. M., Boschi L., Grand S. P. GyPSuM: a joint tomographic model of mantle density and seismic wave speeds. *J. Geophys. Res.: Solid Earth* **115**, (2010).
30. Merdith, A. S. et al. Extending full-plate tectonic models into deep time: linking the Neoproterozoic and the Phanerozoic. *Earth-Sci. Rev.* **214**, (2021).
31. Koelemeijer, P., Deuss, A. & Ritsema, J. Density structure of Earth's lowermost mantle from Stoneley mode splitting observations. *Nat. Commun.* **8**, 15241 (2017).
32. Lau, H. C. P. et al. Tidal tomography constrains Earth's deep-mantle buoyancy. *Nature* **551**, 321–326 (2017).
33. Lekic, V., Cottaar, S., Dziewonski, A. & Romanowicz, B. Cluster analysis of global lower mantle tomography: a new class of structure and implications for chemical heterogeneity. *Earth Planet. Sci. Lett.* **357–358**, 68–77 (2012).
34. Hope, A. C. A. A simplified Monte Carlo significance test procedure. *J. R. Stat. Soc.: Ser. B (Methodological)* **30**, 682–598 (1968).
35. Massey, F. J. The Kolmogorov-Smirnov test for goodness of fit. *J. Am. Stat. Assoc.* **46**, 68–78 (1951).
36. Casella, G. & Berger, R. L. *Statistical Inference* (Thomson Learning; Duxbury Press, Belmont, CA, 2002).
37. Hassan, R., Flament, N., Gurnis, M., Bower, D. J. & Müller, D. Provenance of plumes in global convection models. *Geochem. Geophys. Geosyst.* **16**, 1465–1489 (2015).
38. Cao, X., Flament, N. & Müller, R. D. Coupled evolution of plate tectonics and basal mantle structure. *Geochem. Geophys. Geosyst.* **22**, (2021).
39. Hill, R. I. Mantle plumes and continental tectonics. *Lithos* **30**, 193–206 (1993).
40. Eldholm, O. & Coffin, M. F. Large igneous provinces and plate tectonics. *Geophys. Monogr.-Am. Geophys. Union* **121**, 309–326 (2000).
41. Coffin, M. F. & Coffin, M. Kerguelen hotspot magma output since 130 Ma. *J. Petrol.* **43**, 1121–1137 (2002).
42. Müller, R. D. et al. GPlates: building a virtual earth through deep time. *Geochem. Geophys. Geosyst.* **19**, 2243–2261 (2018).
43. Zhong, S., McNamara, A., Tan, E., Moresi, L. & Gurnis, M. A benchmark study on mantle convection in a 3-D spherical shell using CitcomS. *Geochem. Geophys. Geosyst.* **9**, 1525–2027 (2008).
44. Bower, D. J., Gurnis, M. & Flament, N. Assimilating lithosphere and slab history in 4-D Earth models. *Phys. Earth Planet. Inter.* **238**, 8–22 (2015).
45. Gurnis, M. et al. Plate tectonic reconstructions with continuously closing plates. *Comput. Geosci.* **38**, 35–42 (2012).
46. Coltice, N., Gérault, M. & Ulvrová, M. A mantle convection perspective on global tectonics. *Earth-Sci. Rev.* **165**, 120–150 (2017).
47. Chopelas, A. & Boehler, R. Thermal expansivity in the lower mantle. *Geophys. Res. Lett.* **19**, 1983–1986 (2012).
48. Jaupart, C., Labrosse, S., Lucaleau, F. & Mareschal, J.-C. Temperatures, heat and energy in the mantle of the Earth. In *Treatise on Geophysics* (ed. Schubert, G.) 253–303 (Elsevier, 2015).
49. Adam, M. & Dziewonski, D. L. A. Preliminary reference Earth model. *Elsevier* **25**, 297–356 (1981).
50. Stadler, G. G. et al. The dynamics of plate tectonics and mantle flow: from local to global scales. *Science* **329**, 1033–1038 (2010).
51. Bergeron, S. Y., Yuen, D. A. & Vincent, A. P. Capabilities of 3-D wavelet transforms to detect plume-like structures from seismic tomography. *Geophys. Res. Lett.* **27**, 3433–3436 (2000).
52. Wessel, P. et al. The generic mapping tools version 6. *Geochem. Geophys. Geosyst.* **20**, 5556–5564 (2019).
53. Hunter, J. D. Matplotlib: a 2D graphics environment. *Comput. Sci. Eng.* **9**, 90–95 (2007).

Acknowledgements

A.C. and N.F. were supported by the Australian Research Council grant LP220100056 and N.C. was supported by Australian Research Council grant DP190100180. This research was undertaken with the assistance of resources from the National Computational Infrastructure (NCI), supported by the Australian Government. The University of Wollongong (UOW) also supported access to NCI for the duration of the research. David Evans suggested the acronym 'BLOBS' for 'Big Lower-mantle Basal Structures'.

Author contributions

Annalise Cucchiaro: Conceptualization, methodology, software, validation, formal analysis, investigation, writing—original draft and editing, visualization. Nicolas Flament: Conceptualization, methodology, validation, writing—review and editing, data curation, resources, supervision, project administration, funding acquisition. Maëlis Arnould: Methodology, software, writing—review and editing. Noel Cressie: Conceptualization, methodology, writing—review and editing.

Competing interests

The authors declare no competing interests.

Additional information

Supplementary information The online version contains supplementary material available at <https://doi.org/10.1038/s43247-025-02482-z>.

Correspondence and requests for materials should be addressed to Annalise Cucchiaro.

Peer review information *Communications Earth & Environment* thanks James Panton and the other, anonymous, reviewer(s) for their contribution to the peer review of this work. Primary Handling Editors: Gareth Roberts and Carolina Ortiz Guerrero. A peer review file is available.

Reprints and permissions information is available at <http://www.nature.com/reprints>

Publisher's note Springer Nature remains neutral with regard to jurisdictional claims in published maps and institutional affiliations.

Open Access This article is licensed under a Creative Commons Attribution-NonCommercial-NoDerivatives 4.0 International License, which permits any non-commercial use, sharing, distribution and reproduction in any medium or format, as long as you give appropriate credit to the original author(s) and the source, provide a link to the Creative Commons licence, and indicate if you modified the licensed material. You do not have permission under this licence to share adapted material derived from this article or parts of it. The images or other third party material in this article are included in the article's Creative Commons licence, unless indicated otherwise in a credit line to the material. If material is not included in the article's Creative Commons licence and your intended use is not permitted by statutory regulation or exceeds the permitted use, you will need to obtain permission directly from the copyright holder. To view a copy of this licence, visit <http://creativecommons.org/licenses/by-nc-nd/4.0/>.

© The Author(s) 2025